Research Article Vol. 32, No. 2 / 15 Jan 2024 / Optics Express 2015
Optics EXPRESS

Radiation effect on silicon photonics chips for space quantum key distribution

ZHAO-YUAN CHEN,[1,2] YAN-FEI LIU,[1,3] CHENG CHEN,[1] YANG GAO,[1] AND HAO ZHENG[1]

[1]*Xi'an Research Institute of High Technology, Xi'an 710025, China*
[2]*zhaoyuanchen@outlook.com*
[3]*bbmcu@126.com*

Abstract: Quantum communication satellites have potential for applications in future quantum networks. Photonics integrated chips, due to their compact and lightweight nature, are well-suited for satellite deployment. However, the harsh radiation environment of space can cause permanent damage to these chips, resulting in degraded performance or complete loss of functionality. In this work, we conducted a series of radiation experiments to evaluate the effects of γ rays and high energy protons on quantum key distribution transmitter chips. The results suggest that the insertion loss of the chip is slightly reduced by about 1.5 dB after 100 krad (Si) γ ray irradiation, and further reduced by about 0.5 to 1 dB after $2.39 \times 10^{11}/\text{cm}^2$ proton radiation. The half-wave voltages, extinction ratios, and polarization angles are not changed significantly within the measurement error range. Our work proves the feasibility of deploying quantum constellations utilizing terminals based on photonics chips.

© 2024 Optica Publishing Group under the terms of the Optica Open Access Publishing Agreement

1. Introduction

Global quantum key distribution (QKD) networks have the potential to enable secure data transfer over long distances, leveraging the principles of quantum physics [1,2]. A comprehensive quantum network should be capable of addressing different levels of application scenarios. For urban or intercity communication, quantum communication can leverage classical optical fiber networks. However, for communication distances across continents, the efficiency of optical fiber networks is hampered due to fiber attenuation. In such conditions, satellite-based quantum communication holds a distinct advantage. By harnessing the power of satellites, QKD networks can transcend geographical barriers and provide a secure communication approach for users. In 2016, China launched the quantum communication satellite *Micius*, which has since served as a platform for numerous large-scale quantum experiments. These experiments have demonstrated satellite-to-ground quantum key distribution (QKD) [3,4], entanglement distribution [5–7], and satellite-relayed intercontinental quantum networks [8]. Thanks to quantum satellites, secure communication can now be extended to distances of thousands of kilometers, making long-distance relay of quantum metropolitan-area networks possible [9]. These works represent a large-scale quantum network blueprint that requires a quantum constellation composed of multiple satellites to achieve global coverage and continuous communication. Micro- and Nano-satellites, due to their compact size and lightweight design are the most cost-effective means of establishing a series of quantum nodes in space. To this end, many institutions and companies have initiated quantum nano-satellite projects [10–16].

Photonics integrated chips (PICs) were first used in the field of optical communication and were soon applied to the field of QKD. Several experiments have demonstrated excellent performance of PICs in various application environments, including high-speed transmitters [17–21] and multi-channel receivers [22,23] within fiber networks [24–27] and free-space links [28]. The high level of integration is the most significant advantage of PICs, as it allows for the realization of compact QKD transmitter modules [29] and systems [30]. For this reason, PICs are well-suited

#507260 https://doi.org/10.1364/OE.507260
Journal © 2024 Received 3 Oct 2023; revised 15 Dec 2023; accepted 27 Dec 2023; published 5 Jan 2024

Optics EXPRESS

for use in micro- and nano-satellite applications. However, to date, none of the satellites have carried a QKD-PIC. One of the main challenges in using PICs in space is the potential radiation effects of high-energy solar protons. High-energy particles can cause damage to optoelectronic devices, affecting their performance and on-orbit lifetime [31,32]. To verify the performance changes of various integrated photonics devices in space, researchers have conducted experiments to test their response to total ionizing dose (TID) and high-energy particle displacement damage. These experiments have been conducted on different types of integrated photonics devices, including passive devices [33–38], modulators [39–43], and photodiodes [44,45]. Indeed, most of the research in this area has focused on the performance of individual integrated photonics devices and the effects of single types of irradiation. However, a typical QKD-PIC consists of multiple modules, each containing various building blocks, such as waveguides, multi-mode interferometers (MMIs), and gratings. Furthermore, there are two types of radiation in satellites' operating environment, and it is essential to ensure that QKD-PICs can withstand radiation damage from these sources. Therefore, more research is needed to investigate the effects of two types of radiation on the performance of QKD-PICs and to develop techniques to mitigate any damage caused. Such research is critical for the successful development and deployment of quantum communication networks in space, as it will ensure the reliability and durability of QKD-PICs under challenging conditions encountered in space.

In this study, we conducted a series of radiation experiments on QKD transmitter PICs and evaluated their performance after exposure to different doses of γ-ray and high-energy proton radiation to simulate TID and displacement damage effects. Our findings demonstrate that the QKD transmitter PICs retained their function and performance after receiving 100 kard (Si) γ-ray and 2.39 $\times 10^{11}$/cm^2 proton radiation, which can meet the irradiation dose requirements of the satellite in low Earth orbits [46–48].

2. Experimental setup

2.1. Photonics integrated chips

To ensure the success of quantum communication satellite, the QKD terminal must possess high reliability and stability. To this end, we propose a QKD-PIC using polarization encoding as a transmitter based on silicon photonics technology [29]. Figure 1(a) is the chip structure diagram. This chip was manufactured by a commercial silicon photonics foundry based on a 180 nm silicon-on-insulator (SOI) process. This circuit incorporates both intensity and polarization encoding modules necessary for decoy-state BB84 and MDI (measurement-device-independent) protocols. The QKD transmitter chip consists of three Mach-Zehnder interferometers (MZI), one acting as an intensity modulator (IM) and the other two as two-stage polarization modulators (PM). The chip utilizes the thermo-optic modulators (TOM) and carrier depletion modulators (CDM) as phase shifters and high-speed encoding modulators, respectively. The grating coupler (GC) and two-dimensional grating coupler (2DGC) are used to couple light in and out of the chip. The 2DGC also functions as a polarization combiner, preparing various polarization states according to the encoded phase. Three monitor photodiodes (MPD) are used to monitor the optical power after IM and PM1. All these components are condensed onto a silicon substrate within an area of $3 \times 4.8\ mm^2$. The microscopic image of the QKD-PIC is also displayed in Fig. 1(b).

The critical performance metrics of the QKD transmitter are insert loss (IL), intensity extinction ratio (ER), polarization angle, and half-wave voltage (HWV). IL is the fundamental character of PICs, which directly impacts the output power in a fixed QKD system. ER of the IM will influence decoy state preparation, especially the mean photon number of vacuum pulses. The angle between prepared polarization states is an essential index to evaluate the quantum bit error rate (QBER) of a polarization encoding QKD source. The closer the angle is to 180°, the

Optics EXPRESS

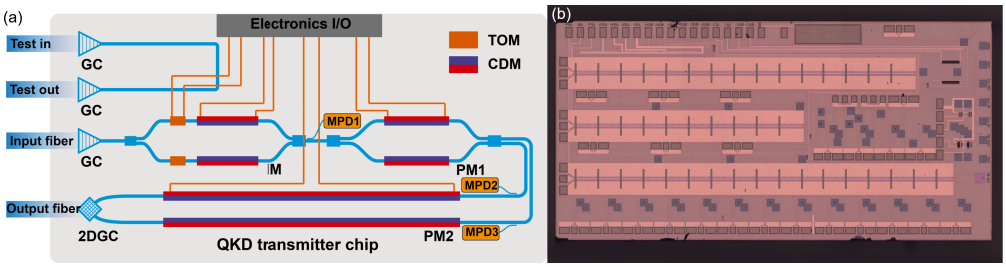


Fig. 1. (a) Structure illustration of the QKD transmitter chips. Grating coupler (GC) and two-dimensional grating coupler (2DGC) serve as optical I/O. The test in and out ports are used for waveguide test. Thermo-optic modulators (TOM) and carrier depletion modulator (CDM) are essential devices to constitute intensity modulator (IM) and two-stage polarization modulator (PM). Monitor photodiodes (MPD) are used to monitor the optical power. (b) Microscope picture of the QKD-PIC.

closer the QBER is to 0%. Half-wave voltage is the electronic parameter of modulators, which determines the demand for electronic drivers.

2.2. Performance metrics characterization

To assess whether these parameters have changed after irradiation, we set up an automated performance evaluation platform for QKD transmitter chips, as shown in Fig. 2, and conducted a series of test experiments after each irradiation. A 1550.12 nm laser diode, working in CW mode, is used as a light source. A beam splitter (BS) splits the laser into two beams. One leads to an optical power meter (Keysight N7748A) as reference light. Another is coupled into the device under test (DUT). A programmable DC power supply is used to provide a voltage signal to TOM and CDM on the chip. The output signal of the DUT is coupled into a polarimeter (Thorlabs PAX1000IR2) and powermeter to measure the polarization angle and output power. An amperemeter is used to record the currents of MPDs. A computer controls all instruments to realize automatic voltage sweeping, data recording, and processing.

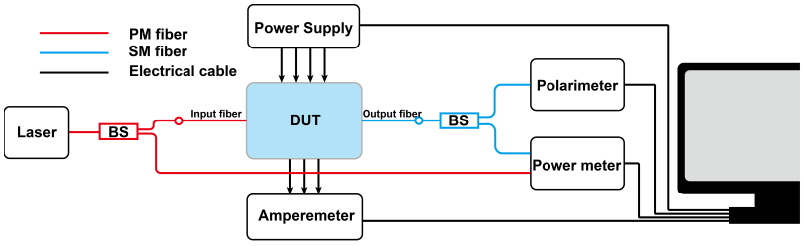


Fig. 2. Automatic performance evaluation platform for QKD transmitter chips. The device under test (DUT) is installed in the system. The power supply provides the drive voltages to the TOM and CDMs on the chip. An amperemeter is used to monitor the currents of MPDs on the chip. The polarimeter and power meter measure the output polarization and power of the chip.

2.3. Sample irradiation

In the actual space environment, there are three sources of radiation influencing satellites, namely, solar cosmic rays (SCR), galactic cosmic rays (GCR), and the van Allen belt [47]. The main sources of Low Earth Orbit (LEO) space radiation that pose a threat to satellites are trapped

Optics EXPRESS

protons and solar protons. For photoelectric devices, high-energy particles mainly cause total ionizing dose effect damage and displacement damage. Hence we performed a series of irradiation experiments to determine radiation damage effects on QKD-PICs performance with different doses. Before experiments, we modeled the radiation environment in LEO and calculated the flux and dose of radiation, using the *Micius* satellite's orbit as an example. The calculation process and results are provided in the Appendix.

Samples S_1 and S_2 were firstly irradiated by a ^{60}Co γ ray source to simulate the TID effect. The dose rate was controlled by setting the distance between the samples and the source. The γ-ray irradiation experiments were conducted four times, and the dose of each experiment was 5, 20, 35, and 40 krad(Si), respectively. After γ irradiation, samples S_1 S_2 together with S_3 and S_4 were irradiated by proton beams in China Spallation Neutron Source (CSNS). Figure 3(a) is a photograph of the proton accelerator in CSNS, and (b) illustrates the proton direction and simple structure. Protons are accelerated over 50 to 70 MeV and then hit the samples vertically to simulate displacement damage caused by high-energy particles in space. We conducted proton radiation experiments three times, and the experimental conditions are listed in Table 1.

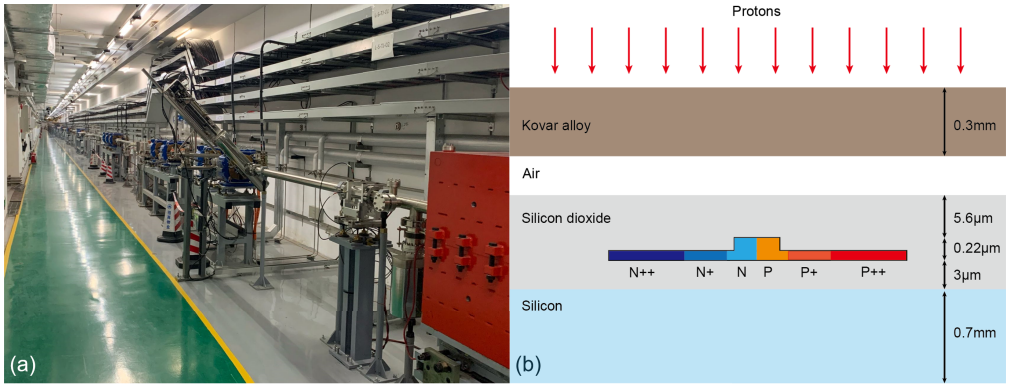


Fig. 3. (a) The proton accelerator in CSNS. (b) Illustration of radiation direction. The chip is packaged by 0.3 mm Kovar alloy.

Table 1. Experiment conditions. The four samples were irradiated according to the experimental conditions from left to right in the table below.

Sample	γ (krad(Si))				Proton (10^{10}/cm^2)		
	5	20	35	40	1.1@50MeV	5.8@60MeV	17@70MeV
S_1	✓	✓	✓	✓	✓	✓	✓
S_2	✓	✓	✓	✓	✓	✓	✓
S_3	-	-	-	-	✓	✓	✓
S_4	-	-	-	-	✓	✓	✓

3. Experimental results

The variation trend of sample IL is shown in Fig. 4. Figure 4(a) is the IL change of samples S_1 and S_2 before and after gamma irradiation. The change trend of the IL of the two samples were almost the same, and both decreased with the increase in radiation dose. After 100 krad (Si) irradiation, IL was reduced by about 1.5 dB. Figure 4(b) indicates that, after proton irradiation, samples' IL also shows a decreasing trend but with different descend ranges. The IL changes of

Optics EXPRESS

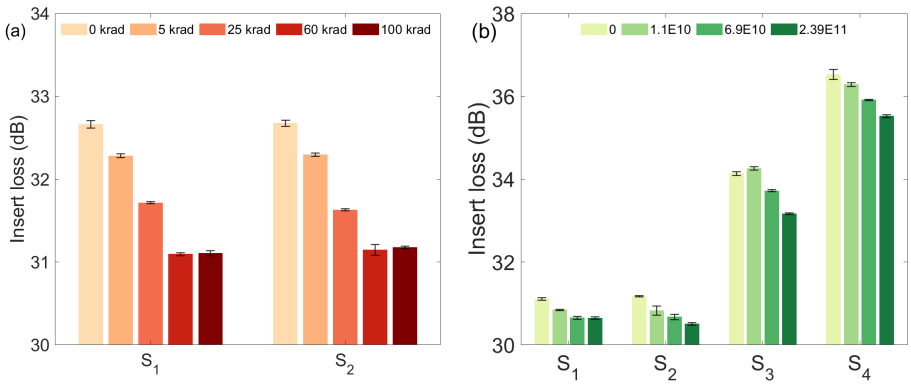


Fig. 4. Insertion loss changes before and after irradiation. Each data point is the mean value of the six sets of measurements, and the error bar is the root mean square of the measured data. The following data is the same. (a) IL change of samples S_1 and S_2 with gamma radiation dose. The red color from light to deep indicates that the cumulative dose increases from 0 krad (Si) to 100 krad (Si), similarly hereinafter. (b) IL change of samples S_1, S_2, S_3, and S_4 with proton radiation dose. The green color from light to deep indicates that the cumulative dose increases from 0 to 2.39×10^{11}/cm^2 protons, similarly hereinafter.

samples S_1 and S_2 are about 0.5 and 0.7 dB, respectively, while S_3 and S_4 have a larger IL change of about 1 dB.

Figure 5 is the HWV after different radiation doses. (a) and (b) are HWVs of sample S_1 with different radiation type and doses, while (d) and (e) are of sample S_2, (c) and (f) are of sample S_3 and S_4, respectively. The HWV measurement results do not show a pronounced change with the irradiation dose like IL. The mean value change of some data is close to the measurement

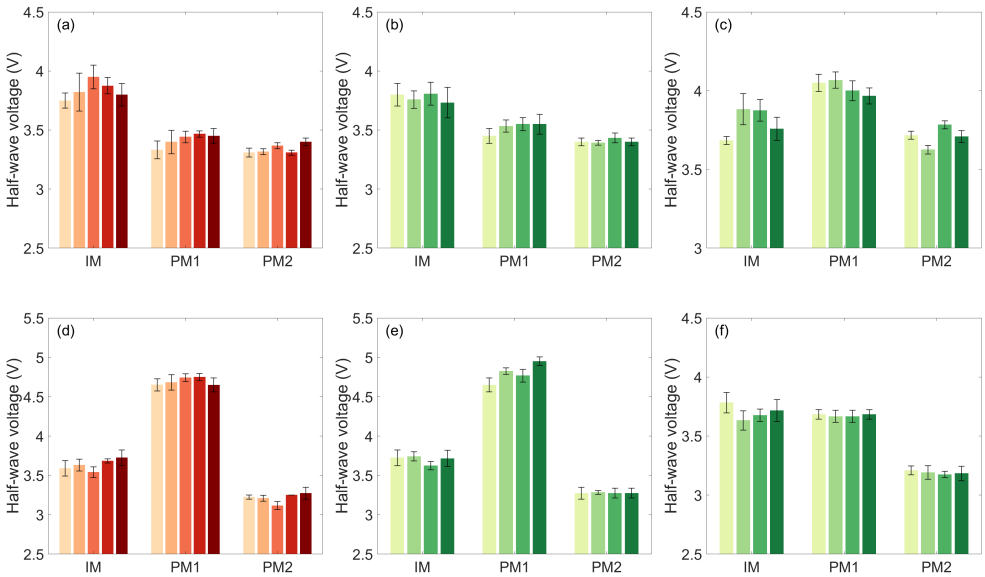


Fig. 5. (a) and (d) are HWVs of sample S_1 and S_2 after γ radiation. (b) and (e) are HWVs of sample S_1 and S_2 after proton radiation. (c) and (f) are HWVs of sample S_3 and S_4 after proton radiation.

Optics EXPRESS

error. For example, in Fig. 5(a), the average IM HWV of S_1 before radiation is 3.75 V with a root-mean-square (RMS) of 0.06 V. After 100 krad (Si) γ ray radiation, the average HWV changes to 3.80 V with a RMS of 0.09 V. The variation of the mean value is only 0.05 V, which is smaller than the measurement error RMS value. Therefore, we believe that under these irradiation doses and conditions, the probability of modulator HWV change is small, and the change range is not obvious.

Figure 6(a), (b), and (c) are ERs of the tested samples, and (d), (e), and (f) are polarization angles of prepared states. The change range of the ER of other samples is within the measurement error range, and there is no significant change trend. The ERs of samples are consistently above 28 dB, which can fully meet the needs of QKD applications. Similarly, the polarization angle prepared by the polarization modulator does not change after irradiation, and all angles are above 170°. Therefore, we believe that there is no obvious deterioration of the modulators after irradiation.

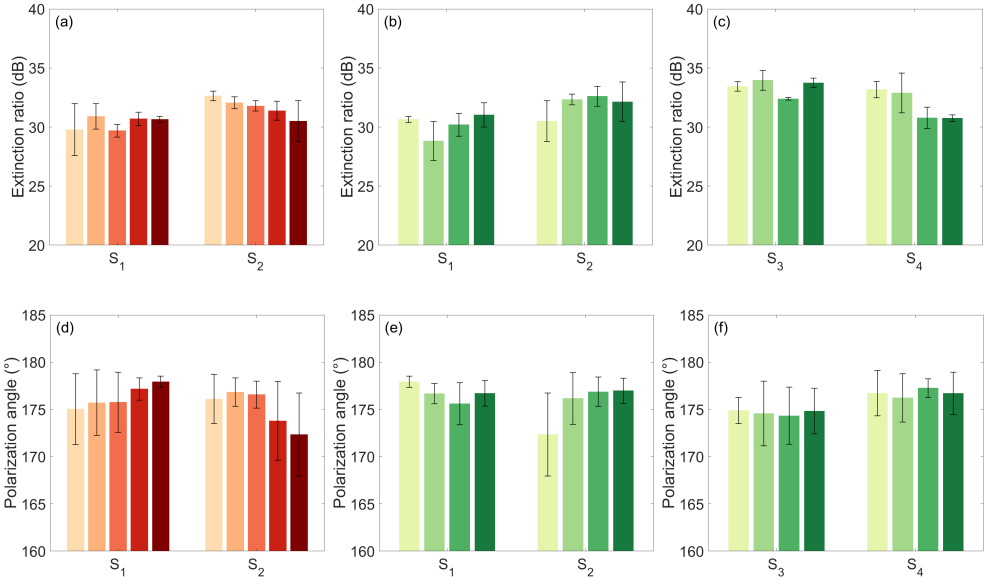


Fig. 6. (a) IM extinction ratio of S_1 and S_2 with γ ray radiation. (b) IM extinction ratio of S_1 and S_2 with proton radiation. (c) IM extinction ratio of S_3 and S_4 with proton radiation. (d) The angle of polarization states prepared by S_1 and S_2 with γ ray radiation. (e) The angle of polarization states prepared by S_1 and S_2 with proton radiation. (f) The angle of polarization states prepared by S_3 and S_4 with proton radiation.

4. Mechanism analysis

4.1. γ ray radiation effect

γ rays have strong penetration capabilities, and based on the data from reference [49], the absorption of gamma rays in 0.3 mm Kovar alloy is approximately 0.013. γ rays with almost no absorption penetrated the packaging material and irradiated the chip. After γ ray irradiation, the IL of the samples shows a decreasing trend. To determine the source of the IL variation, we tested the IL of the test path on the sample, as depicted in Fig. 1(a). The total length of the test optical path (1.2 cm) is slightly shorter than that of the functional optical path (1.7 cm). The IL change of the test optical path before and after irradiation is about 0.2 dB, which is much smaller than that of the functional optical path of 1.5 dB. Therefore, we think that the IL of

Optics EXPRESS

grating and waveguide has little change after irradiation, and the chip IL change is mainly due to the modulator.

Researchers at CERN have done much experimental and theoretical work on silicon photonics modulators within high-dose irradiation environments [39–41,43]. They observed that the modulation efficiency of silicon photonics modulators was significantly reduced after irradiation with a large dose (usually more than 100 Mrad (Si) in large accelerator application scenarios). They attributed this to the ionization of the silica layer by high-energy rays. After silica is ionized, trapped charges are formed at the silica and silicon interface, affecting the concentration distribution of doped carriers inside the modulator. When the dose increases to a certain extent, the doped carriers between the ridge waveguide and slab are entirely squeezed out, resulting in a pinch-off effect, significantly reducing the modulation efficiency. However, their experiments did not evaluate the insertion loss of the modulator.

Based on the device parameters and the methods in the reference [50], we modeled and simulated the modulator before and after irradiation. The width and thickness of the rib waveguide is 500 nm and 220 nm, respectively. The slab thickness is 90 nm. The P- and N-type doping concentrations are 1×10^{18} and 6×10^{17} cm^{-3}. According to references [50,51], the ionizing radiations produce electron-hole (e-h) pairs with a density of $3.7\times10^{16}cm^{-3}krad^{-1}$, and trapped holes are situated within 50-100 Å. Figure 7(a) is the P-type doping profile of the modulator before radiation, while (b) is the profile after 100 krad (Si) radiation. Compared with the pre-irradiation concentration, the doping concentration decreased slightly at 100 krad (Si) irradiation dose. The propagation loss was reduced from 15.1 dB/cm to 14.0 dB/cm at 0 V bias. Because the doping concentration does not change significantly, the modulation efficiency of the modulator under small signals shows no decreasing trend. As the irradiation dose continues to increase up to 10 Mrad (Si), as shown in Fig. 7(c), the doping concentration of the modulator exhibits a pinch-off phenomenon. Only at this point does the modulation efficiency show a significant decrease. In the test samples, the total length of the modulator is 1.25 cm. Hence, the total insertion loss is reduced by 1.4 dB, according to the simulation results. This is very close to the experimental results that the insertion loss reduced by about 1.5 dB after 100 krad (Si) radiation. Therefore, we attribute the change of chip IL to the charge accumulation caused by γ ray ionization affecting the IL of the modulator.

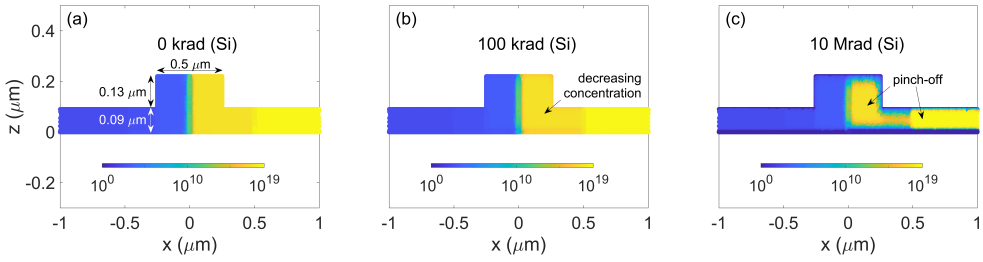


Fig. 7. Simulated P-type doping profile under different radiation doses. (a) Pre-radiation doping profile. (b) Doping profile after 100 krad (Si) dose. The concentration decreases slightly. (c) Doping profile after 10 Mrad (Si) dose. The P-type carriers in waveguide are pinched-off from slab.

4.2. Proton radiation effect

We also observed a decreasing trend of IL after proton radiation. In the process of proton penetrating the sample, ionization damage and displacement damage will be caused. Therefore, we simulated the stopping and range of protons in our simple using SRIM software based on Monte Carlo method [52], then calculated the energy loss and proton distribution profile [53].

Optics EXPRESS

We built a multi-layer material model of the sample, as depicted in Fig. 3(b), and simulated the penetration depth of different proton energies and doses using experimental conditions listed in Table 1. The simulation results are shown in Fig. 8. Figure 8(a) is the proton distribution results, and (b) is the non–ionizing energy loss (NIEL) and ionizing energy loss (IEL) of the three energies protons. Apparently, higher energy protons penetrate deeper, and higher doses leads to higher concentration. The proton distribution of the three energies peaks at 12, 16, and 22 mm, respectively, which far exceeds the thickness of the sample (about 1 mm). This indicates that almost all protons pass through the sample without causing ion implantation effects on the sample. The NIEL of protons increases slowly at the beginning and then reaches its maximum near the peak depth. The IEL of protons is relatively high at the beginning, which is caused by the package metal material, and then follows a similar curve with NIEL but much larger than it. These results suggest that two kinds of damage, i.e., displacement damage and ionization damage, exist simultaneously during proton irradiation, and ionization damage is the majority. Therefore, most of the damage to the samples after high-energy proton irradiation is the TID effect. The change mechanism of chip IL after proton irradiation is the same as γ ray radiation effect.

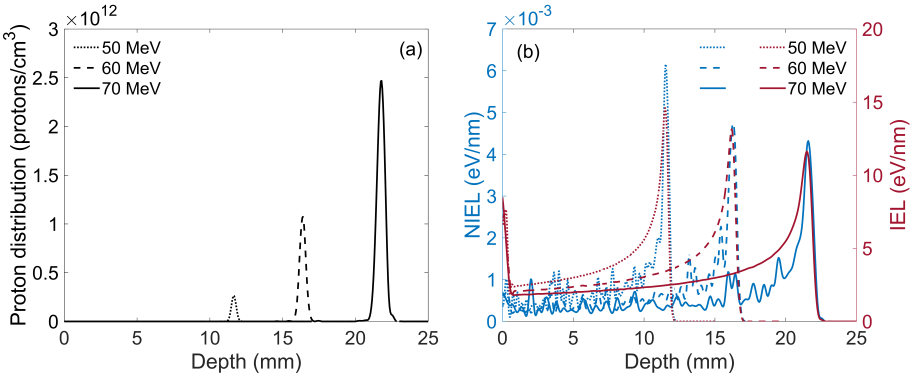


Fig. 8. (a) Simulation results of protons distribution with different energies. (b) NIEL (blue line) and IEL (red line) simulation results. The dotted line, dash line, and solid line represent protons with energy of 50, 60, and 70 MeV, respectively.

5. Security analysis

5.1. Security risk evaluation

Theoretically, the safety of an ideal QKD system is determined by the fundamental laws of quantum physics. But in practice, since the light source is not an ideal single-photon source, it is necessary to introduce decoy state protocol to ensure security [54]. For a fixed QKD system, the experimental parameters in the decoy state protocol are known and unchanging. During the key distribution process, the key extraction is performed using the preset parameters and the actual received photon information. In general, the system parameters do not change, and there are no security vulnerabilities. However, the characteristic changes of QKD-PIC caused by high-energy radiation can lead to inconsistencies between the experimental and the preset parameters. As a result, there is a risk of key leakage.

After radiation experiments, the QKD transmitter chip experiences slightly reduced insert loss. While decreased attenuation might benefit other optical systems, it could pose a potential problem for an isolated QKD system such as a satellite QKD platform. The rate of photons sent per second is carefully calibrated before the satellite launch and is difficult to adjust without extra device installation. If the chip's insert loss is decreased, more photons will be sent than anticipated,

Optics EXPRESS

and eavesdroppers could exploit this opportunity to steal critical information. Therefore, it is necessary to recalculate the system's key rate and evaluate its security.

According to the experimental parameters given in Table 2, we model and calculate the secure key rate (SKR) of a typical decoy state BB84 protocol. In this system, in addition to the signal states (μ), the sender (Alice) also sends two types of decoy states: strong decoy states (ν_1) and weak decoy states (ν_2). The strong decoy states are used to estimate the channel loss, while the weak decoy states are used to check for eavesdropping attempts. The overall signal state photons received by the receiver (Bob) can be expressed as

$$Q_u = Y_0 + 1 - e^{-\eta\mu}, \tag{1}$$

where μ is the number of photons in signal state, Y_0 and η represent background rate and channel loss. The single-photon component of the signal state is considered safe and can be used for key generation. The lower bound gain of single-photon states Q_1 can be estimated by

$$Q_1 \geq \frac{\mu^2 e^{-\mu}}{\mu\nu_1 - \mu\nu_2 - \nu_1^2 + \nu_2^2}(Q_{\nu_1}e^{\nu_1} - Q_{\nu_2}e^{\nu_2} - \frac{\nu_1^2 - \nu_2^2}{\mu^2}(Q_\mu e^\mu - Y_0)), \tag{2}$$

where ν_1 and ν_2 are numbers of photons in strong and weak decoy states. Then, the final key generation rate can be expressed as

$$R \geq \frac{1}{2}(-Q_\mu f_e H_2(E_\mu) + Q_1(1 - H_2(e_1))), \tag{3}$$

where E_μ is the overall QBER, e_1 is the error rate of single-photon states. The key generation rate is related to μ, ν_1, ν_2, and channel loss. We optimize the photon number parameters for each channel loss to obtain the maximum key generation rate. The intrinsic SKR without radiation effects is shown in Fig. 9 (a) with the blue line.

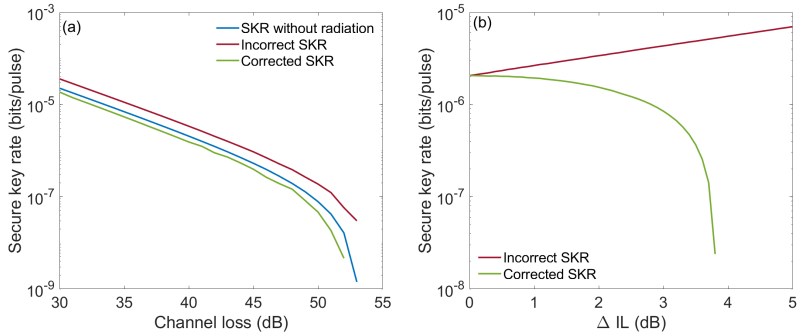


Fig. 9. Simulation results of secure key rate under different conditions. (a) Simulated secure key rate with different channel loss. The blue line is the SKR of the system without IL radiation effect. The red line is the incorrect SKR calculated using a 2 dB IL change due to radiation. The green line is the correct SKR calculated using the modified model. (b) Simulated secure key rate with different IL radiation effects under 40 dB channel loss. The red line is the incorrect SKR without considering the radiation effect. The green line is the corrected SKR calculated using the modified model.

Here, we only consider the influence on IL caused by radiation. According to the experimental results, chip insertion loss is reduced by about 2 dB. If the laser power remains unchanged, the photon number of all states will increase to $\mu' = 10^{0.2}\mu$, $\nu_1' = 10^{0.2}\nu_1$, and $\nu_2' = 10^{0.2}\nu_2$. Therefore, under the same channel attenuation, the number of signal state photons received by

Optics EXPRESS

Table 2. Experimental parameters used in the simulations. The background rate, total misalignment error and detection efficiency are taken from Ref. [29].

Background rate	Y_0	3.2×10^{-7}
Total misalignment error	e_d	1%
Detection efficiency of SNPDs	η_D	30%
Error correction efficiency	f_e	1.12

Bob also increases to

$$Q_{u'} = Y_0 + 1 - e^{-\eta\mu'}. \tag{4}$$

However, if Alice and Bob fail to notice the IL change, they will persist in using Eq. (2) to estimate the lower bound. Consequently, the calculated SKR will be higher than the real SKR, as the red line in Fig. 9(a) reveals. With lower channel loss, the incorrect SKR is approximately 60% higher than the normal SKR without radiation. This difference becomes even more noticeable as the channel loss increases. As a result, a large part of the final keys are insecure keys. To obtain the accurate secure key rate, the parameters in Eq. (2) must be adjusted based on the actual number of photons:

$$Q_1 \geq \frac{\mu'^2 e^{-\mu'}}{\mu'\nu'_1 - \mu'\nu'_2 - \nu'^2_1 + \nu'^2_2}(Q_{\nu'_1}e^{\nu'_1} - Q_{\nu'_2}e^{\nu'_2} - \frac{\nu'^2_1 - \nu'^2_2}{\mu'^2}(Q'_\mu e^{\mu'} - Y_0)). \tag{5}$$

The SKR curve has been corrected and is shown as the green line in Fig. 9(a). The corrected SKR curve is nearly parallel to the typical SKR curve. In the scenario of high attenuation, the corrected SKR experiences a slightly more rapid decrease than the regular rate. The reason for this phenomenon can be attributed to the optimized parameters of the decoy state before irradiation, and the modified parameters deviated from their ideal state post-irradiation. Figure 9(b) shows the incorrect and correct SKR under 40 dB channel loss with different IL changes. Obviously, the wrong key rate will increase slowly with the increase of the IL change, which makes the user misestimate the SKR. However, the correct KR decreases sharply with the rise of IL change. Even when the IL change is greater than 4dB, no secure keys will be obtained. At this time, if users do not realize this problem, they will ultimately lose the security guarantee of quantum communication.

5.2. Countermeasure

Four measures can be taken to avoid safety vulnerabilities caused by radiation exposure. Firstly, radiation protection measures can be implemented to shield the satellite's internal components and reduce their exposure to radiation during orbit. Traditional radiation protection methods often use metal materials, such as aluminium and tantalum, to shield devices and reduce radiation dose. Typically, materials with low secondary radiation are usually selected, such as aluminum and tantalum. Alternatively, a power monitor can be deployed on the satellite to monitor the output optical power of the chip. If the IL of the chip is changed, the key extraction rate equations can be modified to generate the correct SKR and avoid non-secure components. However, this measurement will reduce the final key rate. The third method also needs to deploy a power monitor to monitor the output optical power and then compensate for the loss changes either by adjusting the output power of the laser, or by tuning a variable optical attenuator. Then, the number of photons sent by QKD-PIC is still optimal. This solution only needs to add a simple laser power control function or a variable optical attenuator during the satellite design to avoid the safety risks brought by irradiation, and it will not reduce the secure key rate. The last solution is to use single photon emitters or to operate entanglement protocols, as these frames do not require

Optics EXPRESS

the use of decoy state protocol where precise control over mean photon number is important. And, reducing losses is crucial for improving these systems.

6. Conclusion and discussion

We carried out a series of experimental and theoretical studies to investigate the effect of ionizing radiation on QKD-PIC in space applications. Both TID and displacement damage effects on QKD-PIC are considered. Although the IL of samples has been slightly reduced after γ ray and proton beam irradiation, the essential functions and essential performance of all tested samples show no noticeable change. According to our simulation data, the conditions in our experiments can cover the radiation dose of the satellite in orbit for several years. Our research has accumulated data for the radiation protection design of quantum micro- and nano-satellites and provided a radiation protection scheme from the perspective of security.

In our experimental results, we observed a phenomenon of reduced chip IL after irradiation, which was not observed in previous studies. After simulation and comparison with other works, we conclude that this phenomenon is exhibited by carrier depletion modulators after low-dose irradiation. At a radiation dose of 100 krad (Si), there is a slight change in the doping concentration inside the modulator, resulting in reduced IL. Additionally, under small-signal driving conditions, there is no decrease in modulation efficiency. Although a decrease in IL is generally beneficial for improving device performance, this phenomenon is not desirable in quantum communication satellites employing the decoy state protocol. Firstly, the change in IL, which is unknown to the users, can lead to variations in photon numbers and result in security vulnerabilities. Secondly, as the dose continues to increase, the modulator will eventually exhibit a decrease in modulation efficiency or even complete failure, which may pose risks for future use.

To avoid the security loopholes from IL changes, output power monitor devices and variable optical attenuators should be embedded into the satellite QKD system. However, a number of issues remain to be resolved before the QKD-PIC can be formally deployed on a satellite. Firstly, the effect of radiation protection shields still needs to be verified by experiments further to clarify the relationship between protective measures and radiation doses. The anti-irradiation performance of the monitor used to monitor the power also needs further experimental verification. And the safety risks of variable optical attenuators in QKD systems also need to be further evaluated. Other electro-optical devices in quantum QKD satellites, such as laser diode, quantum random number generator chip, etc., also need to be further assessed for radiation resistance before being deployed on the satellite. In addition, the effects of temperature changes in space also need to be considered. Although there are still many confirmatory experiments and theoretical analyses to be carried out, we still believe that QKD-PIC is one of the first choices for quantum micro- and nano-satellites.

From the perspective of the properties of photonics chips, more detailed research on irradiation characteristics can be further carried out in the future. For example, to study the irradiation effect of low-energy particles (energy is not enough to penetrate samples) on chips. Alternatively, further research could be conducted to investigate the impact of irradiation on the waveguide refractive index. We also indirectly observed the phenomenon of refractive index change in our experiments. Since refractive index is one of the most important properties of optical materials, it is also very valuable to study the change of refractive index properties after irradiation.

Appendix: Modeling and calculations of the radiation environment in the *Micius* satellite orbit

To estimate the radiation dose experienced by low Earth orbit satellites during their operational lifetime, we utilized the SPENVIS tool to model and calculate the radiation environment in the *Micius* satellite's orbit. Figure 10(a) depicts the satellite's orbit trajectory and altitude map. The Micius satellite follows a circular orbit, with its altitudes at 500 km. In this orbit,

Optics EXPRESS

there is a substantial presence of high-energy protons and electrons. Given that electrons have limited penetration capability, our work primarily focuses on the impact of high-energy protons. We calculated the trapped proton and solar proton energy spectra in the orbit using the AP-8 model and the ESP-PSYCHIC model within the SPENVIS tool. We performed interpolation on the calculated results and plotted them in Fig. 10(b). The blue and red curves represent the energy spectra of trapped protons and solar protons, respectively, with it being evident that solar protons constitute the vast majority. The dashed line represents the non-ionizing energy loss of high-energy protons in silicon, with data sourced from reference [55].

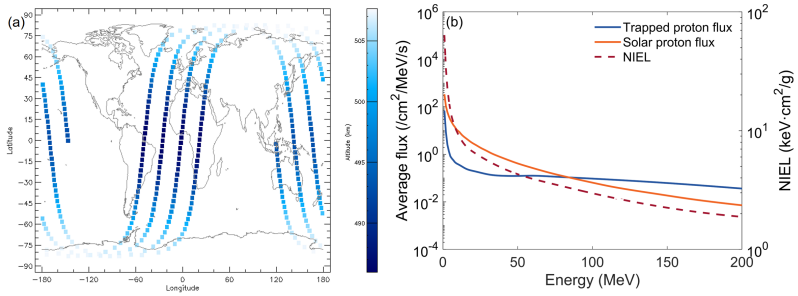


Fig. 10. (a) *Micius* satellite orbit. (b) Proton energy spectra and NIEL.

To calculate displacement damage dose, we used the NIEL value of 10 MeV protons in silicon to calculate the equivalent flux. The proton flux after equivalence is expressed as:

$$F_{tot}^{eq} = \int F(E) \times \frac{NIEL(E)}{NIEL(10)} dE, \tag{6}$$

where F_{tot}^{eq} is the total flux at 10 MeV equivalent, and $F(E)$ is the average flux as shown in Fig. 10(b). Figure 11(a) illustrates the variation of the equivalent proton flux with in-orbit operating time for three different shielding levels. In the *Micius* satellite's orbit, the total proton radiation flux over a twenty-year operational period remains below 10^{11}. The total equivalent flux for three proton irradiation experiments in Table 1, calculated using Eq. (6), is 10^{11}. We use the SHIELDOSE-2 model to calculate the total ionizing dose damage. Figure 11(b) displays the total ionizing radiation dose received by the satellite under three different shielding levels. With shielding of 1mm-thick aluminum or greater, the total ionizing dose received by the satellite over 20 years in orbit is below 100 krad (Si). This indicates that our experimental conditions can support the operational needs of most low Earth orbit satellites for decades.

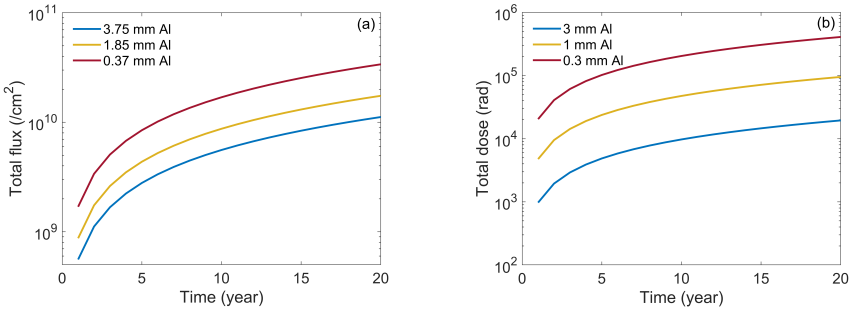


Fig. 11. (a) The total proton flux under three different thicknesses of aluminum shielding. (b) The total radiation dose under three different thicknesses of aluminum shielding.

Optics EXPRESS

Funding. Natural Science Foundation of Shaanxi Province (2022JM-341); National Natural Science Foundation of China (62274182).

Acknowledgments. The authors would like to thank China Spallation Neutron Source and the Heavy Ion Research Facility in Lanzhou for their support of the experiment. Zhao-Yuan Chen would like to thank Cong Wang for the inspiration.

Disclosures. The authors declare that there are no conflicts of interest related to this article.

Data availability. Data underlying the results presented in this paper are not publicly available at this time but may be obtained from the authors upon reasonable request.

References

1. C. H. Bennett and G. Brassard, "Quantum cryptography: Public key distribution and coin tossing," in *International Conference on Computers, Systems, and Signal Processing* (IEEE, 1984), p. 175.
2. C. H. Bennett, F. Bessette, G. Brassard, *et al.*, "Experimental quantum cryptography," J. Cryptology **5**(1), 3–28 (1992).
3. S. K. Liao, W. Q. Cai, W. Y. Liu, *et al.*, "Satellite-to-ground quantum key distribution," Nature **549**(7670), 43–47 (2017).
4. Y. Li, S.-K. Liao, Y. Cao, *et al.*, "Space–ground QKD network based on a compact payload and medium-inclination orbit," Optica **9**(8), 933–938 (2022).
5. J. Yin, Y. Cao, Y. H. Li, *et al.*, "Satellite-based entanglement distribution over 1200 kilometers," Science **356**(6343), 1140–1144 (2017).
6. J. Yin, Y. Cao, Y. H. Li, *et al.*, "Satellite-to-Ground Entanglement-Based Quantum Key Distribution," Phys. Rev. Lett. **119**(20), 200501 (2017).
7. J. Yin, Y. H. Li, S. K. Liao, *et al.*, "Entanglement-based secure quantum cryptography over 1,120 kilometres," Nature **582**(7813), 501–505 (2020).
8. S. K. Liao, W. Q. Cai, J. Handsteiner, *et al.*, "Satellite-Relayed Intercontinental Quantum Network," Phys. Rev. Lett. **120**(3), 030501 (2018).
9. Y. A. Chen, Q. Zhang, T. Y. Chen, *et al.*, "An integrated space-to-ground quantum communication network over 4,600 kilometres," Nature **589**(7841), 214–219 (2021).
10. D. K. L. Oi, A. Ling, G. Vallone, *et al.*, "CubeSat quantum communications mission," EPJ Quantum Technol. **4**(1), 6 (2017).
11. J. A. Grieve, R. Bedington, Z. Tang, *et al.*, "SpooQySats: CubeSats to demonstrate quantum key distribution technologies," Acta Astronaut. **151**, 103–106 (2018).
12. A. Villar, A. Lohrmann, X. Bai, *et al.*, "Entanglement demonstration on board a nano-satellite," Optica **7**(7), 734–737 (2020).
13. H. Podmore, D. Caldwell, S. H. Zheng, *et al.*, "Optical Terminal for Canada's Quantum Encryption and Science Satellite (QEYSSat)," in *International Conference on Space Optical Systems and Applications* (IEEE, 2019), 1.
14. H. Podmore, I. D'Souza, J. Cain, *et al.*, "QKD terminal for Canada's Quantum Encryption and Science Satellite (QEYSSat)," Proc. SPIE **11852**, 118520H (2021).
15. L. Mazzarella, C. Lowe, D. Lowndes, *et al.*, "Quarc: Quantum research cubesat-a constellation for quantum communication," Cryptography **4**(1), 7–25 (2020).
16. I. Mammadov, J. Scharnagl, R. Haber, *et al.*, "Quantum Key Distribution for Secure Communication by Nano-Satellites," in *73th International Astronautical Congress* (2022).
17. C. Ma, W. D. Sacher, Z. Tang, *et al.*, "Silicon photonic transmitter for polarization-encoded quantum key distribution," Optica **3**(11), 1274 (2016).
18. P. Sibson, C. Erven, M. Godfrey, *et al.*, "Chip-based quantum key distribution," Nat. Commun. **8**(1), 13984 (2017).
19. J. E. Kennard, P. Sibson, S. Stanisic, *et al.*, "Integrated silicon photonics for high-speed quantum key distribution," Optica **4**(2), 172–777 (2017).
20. T. K. Paraïso, I. De Marco, T. Roger, *et al.*, "A modulator-free quantum key distribution transmitter chip," npj Quantum Inform. **5**(1), 42 (2019).
21. K. Wei, W. Li, H. Tan, *et al.*, "High-speed measurement-device-independent quantum key distribution with integrated silicon photonics," Phys. Rev. X **10**(3), 031030 (2020).
22. L. Kong, Z. Li, C. Li, *et al.*, "Photonic integrated quantum key distribution receiver for multiple users," Opt. Express **28**(12), 18449 (2020).
23. W. Pernice, F. Beutel, F. Brückerhoff-Plückelmann, *et al.*, "Fully Integrated Four-Channel Wavelength-Division Multiplexed QKD Receiver," Optica **9**(10), 1121–1130 (2022).
24. Y. Ding, D. Bacco, K. Dalgaard, *et al.*, "High-dimensional quantum key distribution based on multicore fiber using silicon photonic integrated circuits," npj Quantum Inform. **3**(1), 25 (2017).
25. D. Bunandar, A. Lentine, C. Lee, *et al.*, "Metropolitan Quantum Key Distribution with Silicon Photonics," Phys. Rev. X **8**(2), 021009 (2018).
26. G. Zhang, J. Y. Haw, H. Cai, *et al.*, "An integrated silicon photonic chip platform for continuous-variable quantum key distribution," Nat. Photonics **13**(12), 839–842 (2019).

Optics EXPRESS

27. H. Semenenko, P. Sibson, A. Hart, *et al.*, "Chip-based measurement-device-independent quantum key distribution," Optica **7**(3), 238–242 (2020).
28. M. Avesani, L. Calderaro, M. Schiavon, *et al.*, "Full daylight quantum-key-distribution at 1550 nm enabled by integrated silicon photonics," npj Quantum Inform. **7**(1), 93 (2021).
29. C. X. Zhu, Z. Y. Chen, Y. Li, *et al.*, "Experimental Quantum Key Distribution with Integrated Silicon Photonics and Electronics," Phys. Rev. Appl. **17**(6), 064034 (2022).
30. T. K. Paraïso, T. Roger, D. G. Marangon, *et al.*, "A photonic integrated quantum secure communication system," Nat. Photonics **15**(11), 850–856 (2021).
31. Y. C. Tan, R. Chandrasekara, C. Cheng, *et al.*, "Silicon avalanche photodiode operation and lifetime analysis for small satellites," Opt. Express **21**(14), 16946 (2013).
32. J. G. Lim, E. Anisimova, B. L. Higgins, *et al.*, "Laser annealing heals radiation damage in avalanche photodiodes," EPJ Quantum Technol. **4**(1), 11 (2017).
33. V. Brasch, Q.-F. Chen, S. Schiller, *et al.*, "Radiation hardness of high-Q silicon nitride microresonators for space compatible integrated optics," Opt. Express **22**(25), 30786 (2014).
34. S. Bhandaru, S. Hu, D. M. Fleetwood, *et al.*, "Total ionizing dose effects on silicon ring resonators," IEEE Trans. Nucl. Sci. **62**(1), 323–328 (2015).
35. F. Morichetti, S. Grillanda, S. Manandhar, *et al.*, "Alpha Radiation Effects on Silicon Oxynitride Waveguides," ACS Photonics **3**(9), 1569–1574 (2016).
36. S. Grillanda, V. Singh, V. Raghunathan, *et al.*, "Gamma radiation effects on silicon photonic waveguides," Opt. Lett. **41**(13), 3053 (2016).
37. P. Shekhar, S. Pendharker, H. Sahasrabudhe, *et al.*, "Extreme ultraviolet plasmonics and Cherenkov radiation in silicon," Optica **5**(12), 1590 (2018).
38. N. Boynton, M. Gehl, C. Dallo, *et al.*, "Gamma radiation effects on passive silicon photonic waveguides using phase sensitive methods," Opt. Express **28**(23), 35192 (2020).
39. S. Seif El Nasr-Storey, F. Boeuf, C. Baudot, *et al.*, "Effect of radiation on a Mach-Zehnder interferometer silicon modulator for HL-LHC data transmission applications," IEEE Trans. Nucl. Sci. **62**(1), 329–335 (2015).
40. M. Zeiler, S. S. El Nasr-Storey, S. Detraz, *et al.*, "Radiation Damage in Silicon Photonic Mach-Zehnder Modulators and Photodiodes," IEEE Trans. Nucl. Sci. **64**(11), 2794–2801 (2017).
41. A. Kraxner, S. Detraz, L. Olantera, *et al.*, "Investigation of the influence of temperature and annealing on the radiation hardness of silicon Mach-Zehnder modulators," IEEE Trans. Nucl. Sci. **65**(8), 1624–1631 (2018).
42. C. Han, Z. Hu, Y. Tao, *et al.*, "Proton radiation effects on high-speed silicon Mach-Zehnder modulators for space application," Sci. China Inf. Sci. **65**(12), 222401 (2022).
43. M. Lalovic, C. Scarcella, A. Bulling, *et al.*, "Ionizing Radiation Effects in Silicon Photonics Modulators," *Transactions on Nuclear Science* pp. 1–6 (IEEE, 2022).
44. G. B. Hoffman, M. Gehl, N. J. Martinez, *et al.*, "The effect of gamma radiation exposure on active silicon photonic device performance metrics," IEEE Trans. Nucl. Sci. **66**(5), 801–809 (2019).
45. K. A. Dean, E. J. Skogen, A. L. Lentine, *et al.*, "Sandia's Radiation-Tolerant Silicon and InP Photonics Platforms with Multi-Project Wafer Runs," Gomactech **m**, 613–617 (2019).
46. B. R. Bhat, N. Upadhyaya, and R. Kulkarni, "Total radiation dose at geostationary orbit," IEEE Trans. Nucl. Sci. **52**(2), 530–534 (2005).
47. M. A. Xapsos, P. M. Neill, and T. P. Brien, "Near-Earth space radiation models," IEEE Trans. Nucl. Sci. **60**(3), 1691–1705 (2013).
48. J. E. Naugle and D. A. Kniffen, "Flux and energy spectra of the protons in the inner Van Allen belt," Phys. Rev. Lett. **7**(1), 3–6 (1961).
49. S. Shimizu, T. Hanai, and S. Okamoto, "The Absorption of Gamma-Rays from Co 60," Phys. Rev. **85**(2), 290–294 (1952).
50. F. De Leonardis, B. Troia, C. E. Campanella, *et al.*, "Modeling of radiation effects in silicon photonic devices," IEEE Trans. Nucl. Sci. **62**(5), 2155–2168 (2015).
51. V. Vasudevan and J. Vasi, "A two-dimensional numerical simulation of oxide charge buildup in MOS transistors due to radiation," IEEE Trans. Electron Devices **41**(3), 383–390 (1994).
52. J. F. Ziegler, M. D. Ziegler, and J. P. Biersack, "SRIM - The stopping and range of ions in matter (2010)," Nucl. Instrum. Methods Phys. Res., Sect. B **268**(11-12), 1818–1823 (2010).
53. S. R. Messenger, "Nonionizing energy loss (NIEL) for heavy ions," IEEE Trans. Nucl. Sci. **46**(6), 1595–1602 (1999).
54. X. Ma, B. Qi, Y. Zhao, *et al.*, "Practical decoy state for quantum key distribution," Phys. Rev. A **72**(1), 012326 (2005).
55. I. Jun, M. A. Xapsos, S. R. Messenger, *et al.*, "Proton Nonionizing Energy Loss (NIEL) for Device Applications," IEEE Trans. Nucl. Sci. **50**(6), 1891–1895 (2003).